

# JGR Space Physics

## RESEARCH ARTICLE

10.1029/2019JA026807

### Key Points:

- We conducted the statistical analysis of the horizontal wavenumber spectra of waves in airglow images in Japan, Canada, and Russia
- Differences of horizontal wavenumber spectra at different locations, seasons, and solar activities are quantitatively obtained
- Weak positive correlation of the power between atmospheric gravity waves and medium-scale traveling ionospheric disturbances was observed

### Correspondence to:

S. Kazuo,  
shiokawa@nagoya-u.jp

### Citation:

Tsuchiya, S., Shiokawa, K., Otsuka, Y., Nakamura, T., Yamamoto, M., Connors, M., et al. (2020). Wavenumber spectra of atmospheric gravity waves and medium-scale traveling ionospheric disturbances based on more than 10-year airglow images in Japan, Russia, and Canada. *Journal of Geophysical Research: Space Physics*, 125, e2019JA026807. <https://doi.org/10.1029/2019JA026807>

Received 9 APR 2019

Accepted 26 JAN 2020

Accepted article online 3 FEB 2020

## Wavenumber Spectra of Atmospheric Gravity Waves and Medium-Scale Traveling Ionospheric Disturbances Based on More Than 10-Year Airglow Images in Japan, Russia, and Canada

Satoshi Tsuchiya<sup>1</sup>, Kazuo Shiokawa<sup>1</sup> , Yuichi Otsuka<sup>1</sup> , Takuji Nakamura<sup>2</sup>, Mamoru Yamamoto<sup>3</sup>, Martin Connors<sup>4</sup> , Ian Schofield<sup>4</sup>, Boris Shevtsov<sup>5</sup>, and Igor Poddelsky<sup>5</sup> 

<sup>1</sup>Institute for Space-Earth Environmental Research, Nagoya University, Nagoya, Japan, <sup>2</sup>National Institute of Polar Research, Tachikawa, Japan, <sup>3</sup>Research Institute for Sustainable Humanosphere, Kyoto University, Kyoto, Japan, <sup>4</sup>Athabasca University, Athabasca, Alberta, Canada, <sup>5</sup>Institute of Cosmophysical Researches and Radio Wave Propagation, Far Eastern Branch Russian Academy of Sciences, Vladivostok, Russia

**Abstract** We have studied atmospheric gravity waves (AGWs) and nighttime medium-scale traveling ionospheric disturbances (MSTIDs) by applying three-dimensional spectral analysis technique to 557.7- and 630.0-nm airglow images at Shigaraki (SGK) (35°N, 136°E, 1999–2017) and Rikubetsu (RIK) (44°N, 144°E, 1999–2017), Japan, Athabasca (ATH), Canada, (55°N, 247°E, 2005–2017), and Magadan (MGD), Russia (60°N, 151°E, 2008–2017), focusing on their horizontal wavenumber spectra. For the AGWs in 557.7-nm images, the power spectra in summer are stronger than in other seasons, probably due to stronger tropospheric convection. The highest energy content of the waves are mostly at wavelengths between 20 and 300 km at MGD, ATH, and RIK, while it is above 200 km at SGK. The largest power spectral density is obtained at RIK at wavelengths of 30–100 km and then ATH. The slopes of the horizontal wavenumber spectra varies from  $-2.77$  to  $-3.22$ . From the MSTIDs in 630.0-nm images, the power spectra in summer at RIK and SGK are stronger than those in other seasons regardless of solar activity. The power spectra in solar quiet time are stronger than those in solar active time at all four stations. These features can be explained by the Perkins instability with coupling between sporadic *E* and *F* layers. The spectral slope decreases with increasing latitudes. Weak positive correlations were obtained between the daily wave power of AGWs in 557.7-nm images and MSTIDs in 630.0-nm images, suggesting that the MSTIDs in the thermosphere may be partially generated by the AGWs from the mesopause region.

**Plain Language Summary** In this paper we study atmospheric gravity waves (AGWs) and nighttime medium-scale traveling ionospheric disturbances (MSTIDs) observed at four stations in Japan, Canada, and Russia, in 557.7- and 630.0-nm airglow images over more than 10 years. The 557.7-nm airglow has an emission layer at altitudes of 90–100 km (mesopause region). The waves seen in the 557.7-nm airglow images mainly indicates AGWs. The 630.0-nm airglow has an emission layer at altitudes of 200–300 km (bottomside ionosphere). The waves seen in the 630.0-nm airglow images mainly indicates MSTIDs in the ionosphere. The AGWs in the mesopause region are the main driver of global atmospheric circulation in the middle atmosphere. The MSTIDs in the bottomside ionosphere are one of the causes of the satellite positioning error. We show typical energy content, propagation direction, and wavelengths of these waves at these two altitudes and discuss possible reason of the observed characteristics. These results contribute to our understanding of generation and propagation of AGWs and MSTIDs in the upper atmosphere.

## 1. Introduction

Atmospheric gravity waves (AGWs) transport energy from the troposphere to the upper atmosphere and break at the top of the mesosphere. The breaking waves cause energy deposition in this mesopause region, driving large-scale pole-to-pole circulation and determine the average wind and temperature structure of the Earth's middle atmosphere (e.g., Matsuno, 1982). In particular, short-period AGWs tend to have large influence on the atmospheric dynamics, since the amount of the momentum they transport is large (Vincent, 1984). Medium-scale traveling ionospheric disturbance (MSTID) is a disturbance of the ionospheric plasma density with a period of 15–60 min and wavelength of several hundred kilometers (Hunsucker, 1982). The MSTIDs affect satellite positioning, such as that by Global Positioning System, because the

electromagnetic wave velocity used for the positioning depends on the plasma density in the ionosphere (e.g., Davies, 1990; Tsugawa et al., 2018).

Airglow imager is a powerful tool to obtain two-dimensional images of waves in the upper atmosphere. AGWs and nighttime MSTIDs are typical wave structures seen in 557.7-nm (emission altitude: 90–100 km) and 630.0-nm (200–300 km) airglow images, respectively, at middle latitudes. The horizontal characteristics of AGWs and MSTIDs have been investigated by specifying waves in airglow image through visual inspection by manually analyzing individual images (e.g., Garcia et al., 2000; Hecht et al., 1994; Nakamura et al., 1999; Shiokawa et al., 2003; Taylor & Hapgood, 1988). However, it is difficult to conduct long-term analysis and to compare results obtained at different places, because the visual inspection takes time and the criteria to pick up waves differ depending on each person.

Analysis methods for objectively extracting wave parameters from airglow images have been developed by using the fast Fourier transform (FFT). Hecht et al. (1994) first applied two-dimensional spectral analysis to airglow images and analyzed the wavenumber spectrum in the horizontal direction. With the progress of spectral analysis, three-dimensional (3-D) FFT including the time domain was performed, and the spectrum of horizontal wavenumber and frequency was calculated (Coble et al., 1998). Then, Matsuda et al. (2014) proposed a method to expand the 3-D FFT analysis to estimate the horizontal phase velocity of the waves.

Horizontal characteristics of AGWs have been extensively studied by using airglow images (e.g., Fritts & Alexander, 2003; Hecht et al., 1994; Nakamura et al., 1999; Taylor & Hapgood, 1988; Walterscheid et al., 1999; Yue et al., 2010). Wu and Killeen (1996) showed a seasonal dependence of AGW activity from the airglow images at Michigan during 1993 to 1994. Hecht et al. (1994) have shown that the spectral slope for the two-dimensional horizontal wavenumber of AGWs seen in OH and O<sub>2</sub> airglow images is consistent with the separable model developed by Gardner et al. (1993). Tsuchiya et al. (2018) investigated seasonal and year-to-year variation of the horizontal phase velocity spectra of AGWs by using 3-D FFT analysis techniques on the airglow images at Shigaraki (SGK) (34.8°N, 136.1°E) and Rikubetsu, (RIK) (43.5°N, 143.8°E), Japan, from 1999 to 2014. They concluded that the seasonal difference of the propagation direction of AGWs is probably due to the wind filtering by the mesospheric jet and the location of the wave source relative to the observation site. Tsuchiya et al. (2019) further studied the horizontal phase velocity of AGWs over 10 years obtained at Athabasca (ATH), Canada (54.7°N, 246.7°E and 54.6°N, 246.3°E, 2005–2017), and Magadan (MGD), Russia (60.1°N, 150.7°E, 2008–2017) and compared them with the results at SGK and RIK. However, comparison of characteristics of horizontal wavenumber spectra of AGWs at different locations over 10 years has not yet been conducted.

Nighttime MSTIDs seen in 630.0-nm airglow images have been also extensively studied (e.g., Garcia et al., 2000; Makela & Kelley, 2003; Narayanan et al., 2014; Otsuka et al., 2004; Shiokawa et al., 2003; Taylor et al., 1998). Shiokawa et al. (2003) have reported that the occurrence rate has a major peak in summer with a minor peak in winter by using airglow images observed at Rikubetsu and Shigaraki for 1998–2000. Amorim et al. (2001) studied nighttime MSTIDs in the Brazilian low latitudes over 10.5 years. They have shown that the nighttime MSTIDs have negative correlations to the solar activity. Tsuchiya et al. (2018, 2019) studied the horizontal phase velocity of MSTIDs seen in 630.0-nm airglow images by using 3-D spectral analysis techniques at RIK and SGK, Japan during 1999–2014 and ATH, Canada (2005–2017), and MGD (2008–2017), Russia, respectively. However, comparison of characteristics of horizontal wavenumber spectra of MSTIDs at different locations over 10 years has not yet been conducted.

In this study, we have studied AGWs and nighttime MSTIDs by applying the three-dimensional spectral analysis technique to the 557.7- and 630.0-nm airglow images at SGK and RIK, Japan, ATH, Canada and MGD, Russia. This data set was used in previous reports by Tsuchiya et al. (2018, 2019) for horizontal phase-velocity spectra, but in the present study we focus on their horizontal wavenumber spectra. We examined similarities and differences of these spectra to see their dependence on latitudes and longitudes.

## 2. Method of Analysis

We analyzed the airglow images observed by the cooled charge-coupled device cameras, which are part of the Optical Mesosphere Thermosphere Imagers (OMTIs) operated by the Institute for Space-Earth

**Table 1**  
*Parameter of Airglow Imagers Used in This Study*

	Magadan	Athabasca	Rikubetsu	Shigaraki
station location	60.1°N, 150.7°E	54.7°N, 246.7°E\ (since 25 September 2005) 54.6°N, 246.3°E (from 27 September 2012)	43.5°N, 143.8°E	34.8°N, 136.1°E
analyzed period	4 November 2008 to 27 August 2015 27 December 2016 to 31 December 2017	3 September 2005 to 31 December 2017	21 February 1999 to 31 December 2017	21 February 1999 to 31 December 2017
wavelength	557.7 nm (AGW)\ 630.0 nm (MSTID)	557.7 nm (AGW) 630.0 nm (MSTID)	557.7 nm (AGW) 630.0 nm (MSTID)	557.7 nm (AGW) 630.0 nm (MSTID)
exposure time (557.7 nm)	30 s	5 s	105 s (since 19 May 2008) 30 s (from 20 May 2008)	120 s
exposure time (630.0 nm)	40 s	30 s	165 s (since May 19 2008) 40 s (from May 20 2008)	180 s
time resolution	1.5 min	2.0 min	5.5 min (since May 19 2008) 1.5 min (from May 20 2008)	5.5 min
number of pixels	256	256	512 (since May 19 2008) 256 (from May 20 2008)	512
sky condition	clear sky only	clear sky only	clear sky only	clear sky only

Environmental Research, Nagoya University (Shiokawa et al., 1999, 2009, 2017). The stations used in the present study were MGD, Russia, ATH, Canada, and RIK and SGK, Japan. Table 1 shows the parameters of the airglow imagers used in this study. These imagers obtain airglow images using band-pass filters for OI 557.7 nm, OI 630.0 nm, and background emission at 572.5 nm. Imager #1 has been operated at SGK (34.8°N, 136.1°E, MLAT: 25.4°N) since 1 October 1998. At RIK (43.5°N, 143.8°E, MLAT: 34.7°N), Imager #3 was operated from 1 October 1998 to 19 May 2008, and Imager #9 has been in operation since 19 May 2008. At ATH, Imager #7 has been in operation at 54.7°N, 246.7°E (magnetic latitude [MLAT]: 61.7°N) since 3 September 2005. This imager was moved a short distance (~40 km) to 54.6°N, 246.3°E (MLAT: 61.1°N) on 27 September 2012. At MGD, Imager #11 has been operated at 60.1°N, 150.7°E (MLAT: 51.9°N) since 4 November 2008. Imagers #1 (SGK) and #3 (RIK) obtained airglow images with 512 × 512 pixels every 5.5 min. Imagers #9 (RIK) and #11 (MGD) obtained airglow images with 256 × 256 pixels every 1.5 min, with 2 × 2-pixel binning. Imager #7 (ATH) obtained airglow images with 256 × 256 pixels every 2 min with the binning. We used only the images with clear sky for the present analysis. The clear-sky condition was identified by visual inspection of all-sky airglow images and stored as 1-hr status for all the stations throughout the observation period.

In this study, we applied the 3-D FFT procedure developed by Matsuda et al. (2014) to obtain the two-dimensional horizontal wavenumber spectra. The parameters used for the image processing are the same as the parameters used in Tsuchiya et al. (2018, 2019) with the exception of the image sizes in geographic coordinate at RIK and MGD. We used the 557.7-nm images projected on 200 × 200-km square map in geographic coordinates at RIK and MGD and on 400 × 400 km at SGK and ATH. The 630.0-nm images were projected on 800 × 800-km square maps at SGK, RIK, and ATH, and on 400 × 400 km at MGD. This prevents contamination by the obstacles (lightning rod and the shutter of the imager) from entering the analyzed images.

The absolute intensities of 557.7- and 630.0-nm airglow emission in the images were calculated by subtracting sky background continuum emission which is monitored at a wavelength of 572.5 nm. We calculated the deviation  $\Delta I$  of the airglow intensity  $I$  by the intensity  $I_a$  averaged over the 2- or 4-hr time segment as  $\Delta I = (I - I_a)/I_a$ . For the images with the 1.5- and 2-min time resolution, we subtracted and scaled the airglow intensity from the 2-hr running average. For the 5.5-min time resolution, we subtracted and scaled using the 4-hr running average. The wavenumber spectra were integrated in the frequency domain for 1/11–1/60 (/min).

557.7 nm Solar Active

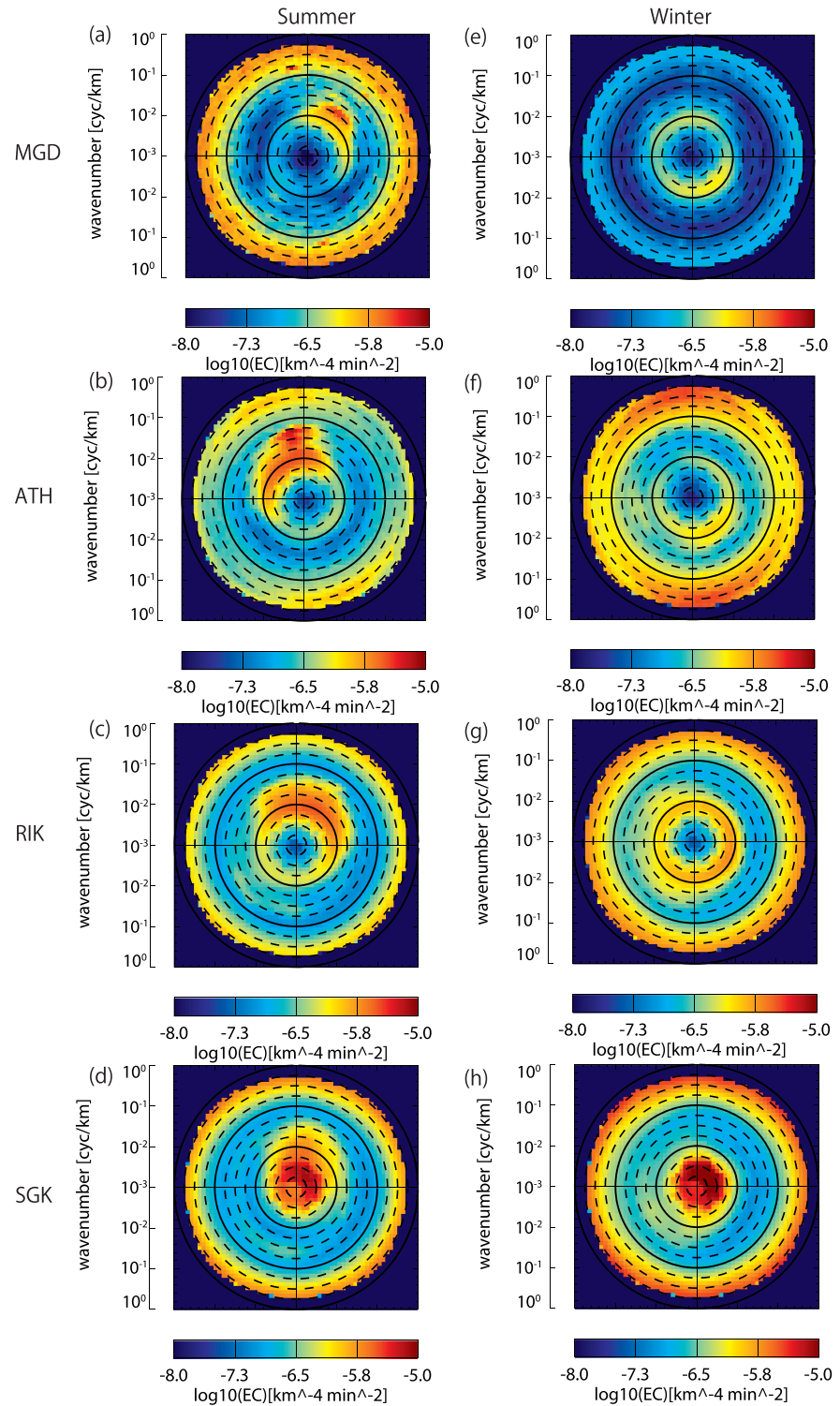


**Figure 1.** Seasonal averages of the energy content (EC) of the horizontal wavenumber of AGWs seen in 557.7-nm airglow images at MGD (a and e), ATH (b and f), RIK (c and g), and SGK (d and h) in summer (a–d) and winter (e and f) in the solar active time (1999–2004 and 2011–2015).

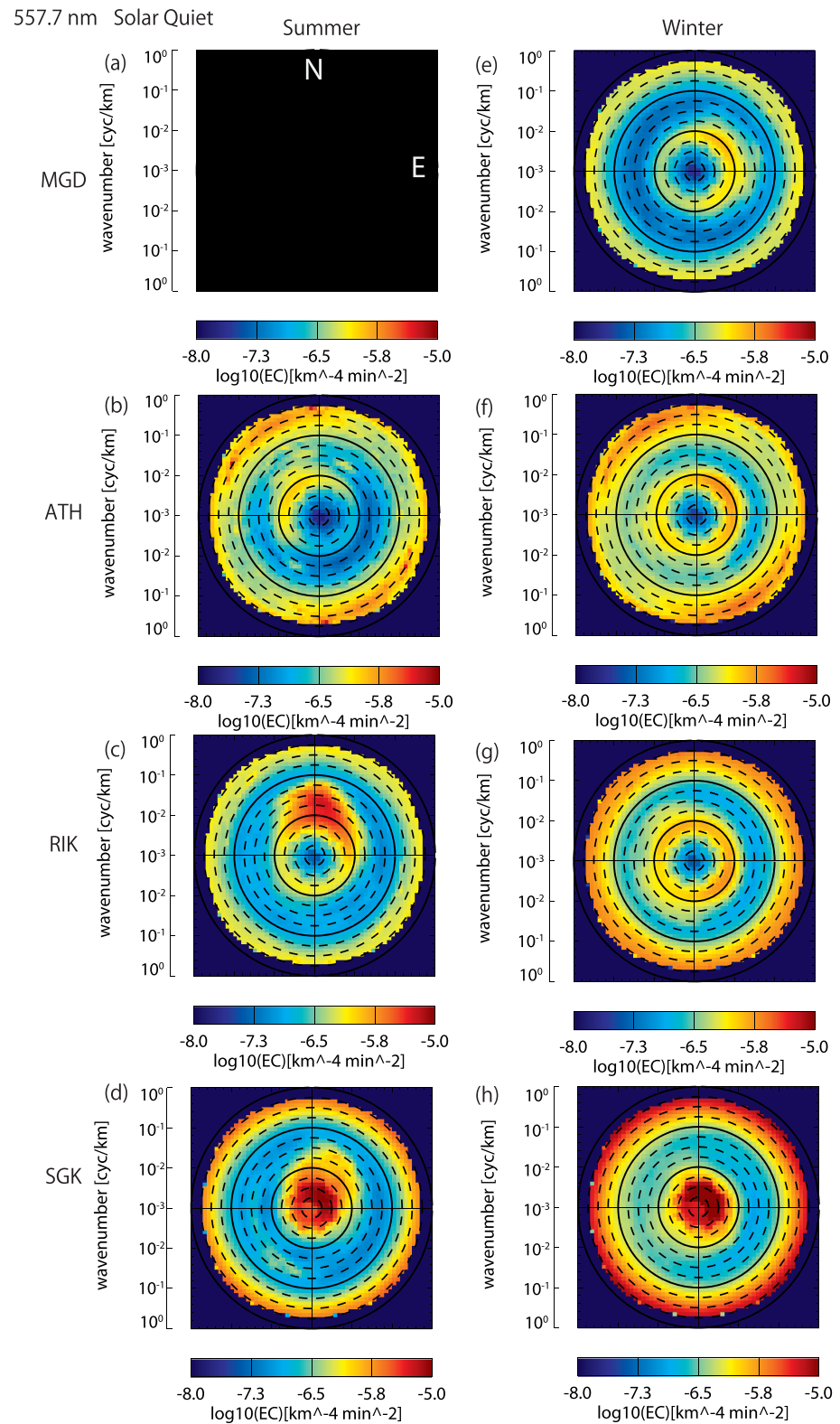


**Figure 2.** Seasonal averages of the energy content (EC) of the horizontal wavenumber of AGWs seen in 557.7-nm airglow images at MGD (a and e), ATH (b and f), RIK (c and g), and SGK (d and h) in summer (a–d) and winter (e and f) in the solar quiet time (2005–2010).

**Table 2**  
Energy Content (EC), Propagation Direction, and Wavelengths of Main EC Peak and Secondary EC Peak in AGW Spectra Shown in Figures 1 and 2

AGW (557.7 nm)	EC in unit of ( $\text{km}^{-4} \cdot \text{min}^{-2}$ )	Solar active (Figure 1)		Solar quiet (Figure 2)	
		Summer	Winter	Summer	Winter
MGD	main EC peak	log <sub>10</sub> (EC): -5.6 NE 20–200 km	log <sub>10</sub> (EC): -6.2 SW-SE 50–100 km	—	log <sub>10</sub> (EC): -5.9 NW-SW 50–200 km
	secondary EC peak	log <sub>10</sub> (EC): -6.8 SW 30–100 km	log <sub>10</sub> (EC): -6.5 N 50–100 km	—	log <sub>10</sub> (EC): -6.3 OMNI 100–200 km
ATH	main EC peak	log <sub>10</sub> (EC): -5.3 NW-N 20–300 km	log <sub>10</sub> (EC): -6.0 S-SE 50–200 km	log <sub>10</sub> (EC): -6.0 NW 30–300 km	log <sub>10</sub> (EC): -5.8 NE 50–300 km
	secondary EC peak	log <sub>10</sub> (EC): -5.5 W 50–200 km	—	log <sub>10</sub> (EC): -6.1 NE-NW-SW 100–200 km	log <sub>10</sub> (EC): -6.0 OMNI 50–200 km
RIK	main EC peak	log <sub>10</sub> (EC): -5.3 NW-NE 20–200 km	log <sub>10</sub> (EC): -5.6 OMNI with slight W preference 50–300 km	log <sub>10</sub> (EC): -5.5 N 20–300 km	log <sub>10</sub> (EC): -5.8 OMNI 50–200 km
	secondary EC peak	—	log <sub>10</sub> (EC): -6.2 SW-NW 30–100 km	log <sub>10</sub> (EC): -6.0 OMNI 100–200 km	log <sub>10</sub> (EC): -6.3 NW-SW 30–100 km
SGK	main EC peak	log <sub>10</sub> (EC): -5.2 NW-NE 20–500 km	log <sub>10</sub> (EC): -5.0 SW-N 200–500 km	log <sub>10</sub> (EC): -5.2 NE 30–500 km	log <sub>10</sub> (EC): -5.0 NE-SE 200–500 km
	secondary EC peak	—	log <sub>10</sub> (EC): -6.4 SW 30–100 km	log <sub>10</sub> (EC): -5.6 OMNI 200–500 km	log <sub>10</sub> (EC): -5.3 OMNI 300–500 km

### 3. Results From the 557.7-nm Airglow Images

Figures 1 and 2 show seasonal averages of distribution of the energy content (EC) of AGWs seen in 557.7-nm airglow images for the horizontal wavenumber space in the solar active time and the solar quiet time, respectively, at MGD (a and e), ATH (b and f), RIK (c and g), and SGK (d and h) in summer (a–d) and winter (e and f). We multiplied the square of the wavenumber ( $k$ ) by the power spectral density (PSD) to calculate the EC ( $\text{EC} = \text{PSD} * k^2$ ) of AGWs. We defined solar active time as 1999–2004 and 2011–2015 and solar quiet time as 2005–2010 from the yearly variation of the  $F10.7$  solar flux shown in Tsuchiya et al. [2018, 2019]. The seasons defined as summer (20 April to 20 August) and winter (20 October to 20 February) are 4 months each centered on the solstice. The wavenumber in the horizontal (east-west) and vertical (north-south) axes are shown in log scale from  $10^0$  (wavelength: 1 km) to  $10^{-3}$  (wavelength: 1,000 km). It should be noted that the EC at wavenumber of more than  $10^{-1}$  ( $\text{km}^{-1}$ ) (wavelength less than 10 km) does not represent the EC of AGWs because of the effect of the white noise in the images, and that the EC at wavenumber of less than  $10^{-2}$  ( $\text{km}^{-1}$ ) (wavelength more than 100 km) suffers from low wavenumber resolution due to limitation of the image size ( $200 \times 200$  km or  $400 \times 400$  km). Table 2 summarizes the EC, propagation direction, and wavelengths for the main EC peak and secondary EC peak in AGW spectra in Figures 1 and 2.

As shown in Table 2, the highest ECs are mostly at wavelengths between 20 and 300 km at MGD, ATH, and RIK, while it is above 200 km at SGK. The ECs are larger in summer than in winter except for SGK, suggesting stronger AGW sources in the lower atmosphere in summer. The propagation direction of AGWs in summer is narrower than those in winter and is always contain northward (poleward) at all the stations in both solar active and quiet time. This poleward preference in summer has been reported by previous literatures and can be caused by duct propagation of AGWs generated near the equatorial troposphere to higher latitudes (e.g., Ejiri et al., 2003; Nakamura et al., 1999; Suzuki et al., 2004, 2013; Takeo et al., 2017; Tsuchiya et al., 2018, 2019; Walterscheid et al., 1999).

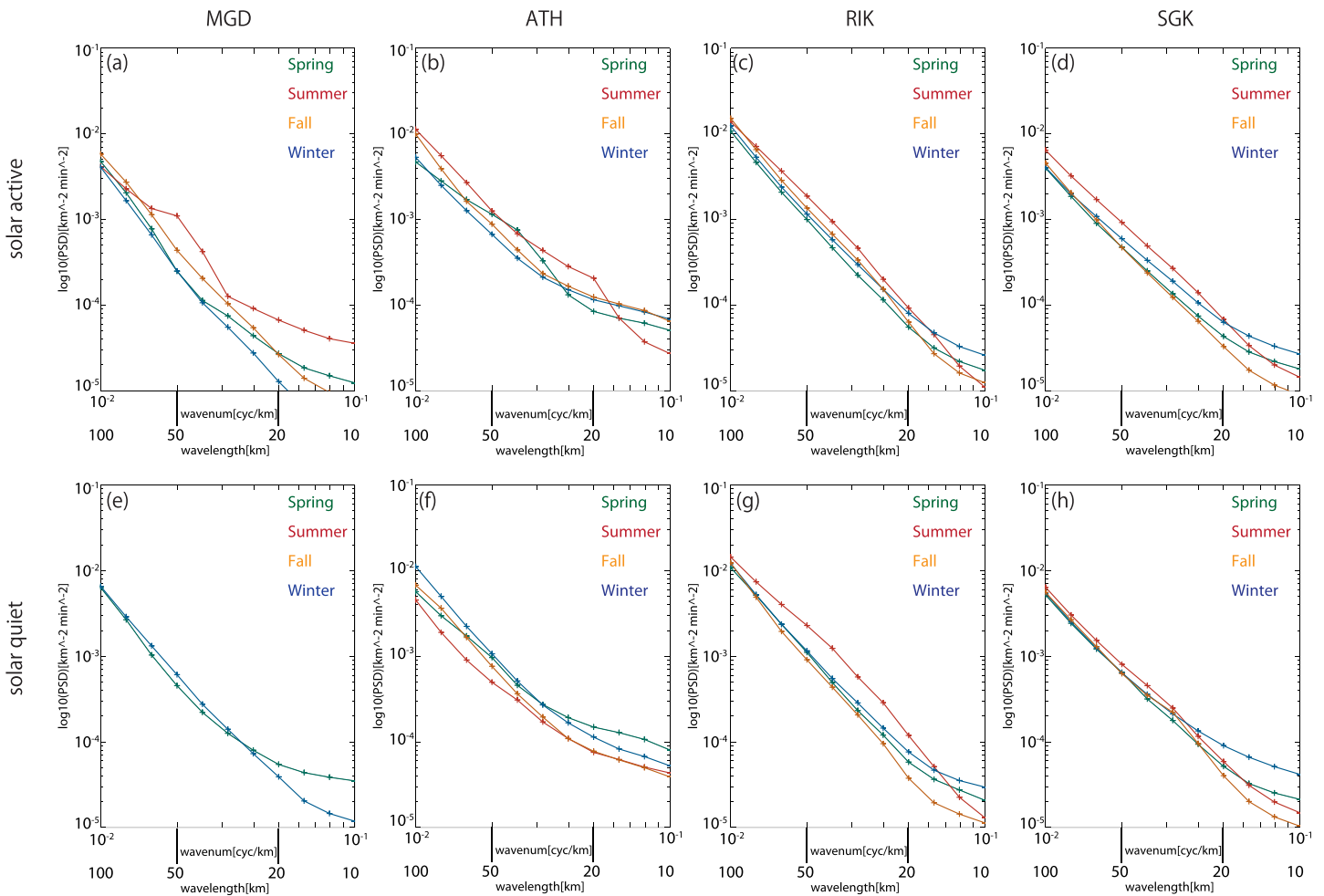


**Figure 3.** Seasonal averages of the horizontal wavenumber spectra of AGWs in 557.7-nm airglow images at MGD (a and e), ATH (b and f), RIK (c and g), and SGK (d and h) in the solar active time (a–d) and the solar quiet time (e–h). The line colors show the seasons as spring (green), summer (red), fall (orange), and winter (blue).

In winter, the propagation direction of AGWs is much broader than that in summer and preference of wave propagation direction tends to become unclear, as shown in Figures 1 and 2. The westward preference of the AGW propagation, which is expected from wind filtering by eastward mesospheric jet in winter and was clear in phase-velocity spectra in Takeo et al. (2017) and Tsuchiya et al. (2018), can be seen as the secondary EC peak at smaller wavenumbers ( $<100$  km) at RIK and SGK, while they are not clear at ATH and MGD. This may be due to weakening of mesospheric jet at these high-latitude stations and relative location to major tropospheric convection sources, as discussed by Tsuchiya et al. (2019) with tropospheric convection maps. There is no discernible difference between solar active time (Figure 1) and solar quiet time (Figure 2) in winter at RIK and SGK. There are slight differences between solar active and quiet time in winter at MGD and ATH in the propagation direction, but the peak ECs and their wavelengths are comparable.

Next we integrated the PSD of each horizontal wavenumber over the azimuthal direction to see the wavenumber distribution of the PSD. We only show the spectra with wavenumbers from  $10^{-2}$  to  $10^{-1}$  (wavelengths from 10 to 100 km) for two reasons: (i) The PSD at wavelengths of more than 100 km was cut out, because the data coverage of  $400 \times 400$  km (or  $200 \times 200$  km) does not include a full wavelength in this range. (ii) The PSD at wavelengths of less than 10 km was cut out, because the waves with horizontal wavelengths of less than 10 km are possibly caused by atmospheric instabilities rather than AGWs, as suggested by for example, Fritts et al. (1997).

Figure 3 shows the seasonal averages of the horizontal wavenumber spectra of AGWs at MGD (a and e), ATH (b and f), RIK (c and g), and SGK (d and h) in the solar active time (a–d) and the solar quiet time (e–h). The

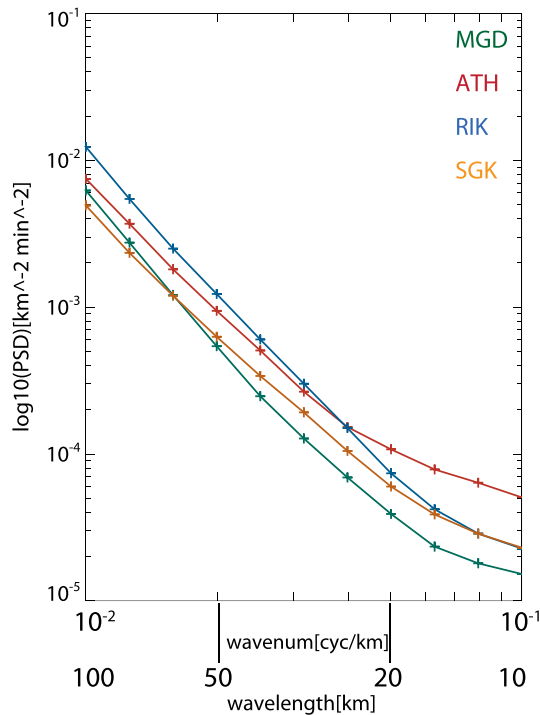


**Figure 4.** Horizontal wavenumber spectra of AGWs in 557.7-nm airglow images at MGD (green), ATH (red), RIK (blue), and SGK (orange) averaged over whole analysis periods.

line colors show the seasons as spring (green), summer (red), fall (orange), and winter (blue). The spring and fall are defined as 2 months each centered on the equinox. The PSD decreases with increasing wavenumbers (decreasing wavelengths), as expected from natural wave distributions. The small-scale AGWs usually have smaller periods, which tend to dissipate at lower atmosphere (e.g., Azeem et al., 2015; Vadas, 2007). The power spectra in summer are stronger than those in other seasons over ~20–100 km at RIK and SGK regardless of solar activity. This tendency can be also seen in ATH and MGD in solar active time.

Figure 4 shows the comparison of the horizontal wavenumber spectra at MGD (green), ATH (red), RIK (blue), and SGK (orange) averaged over the whole analysis periods. The gradient of the power spectra become smaller at wavelength below 20 km. The small-scale wave-like structures in airglow images with scale size of less than 10 km has been suggested as manifestation of atmospheric instabilities (e.g., Fritts et al., 1997). This may be the reason of this gentle gradient in PSD below 20 km in Figure 4. The largest PSD is obtained at RIK at 30–100 km and then ATH follows. The slope of the power spectrum between 20 and 100 km at MGD, ATH, RIK, and SGK is  $-3.22$ ,  $-2.77$ ,  $-3.11$ , and  $-2.68$ , respectively.

#### 4. Discussion of the 557.7-nm Results

As shown in Table 2, the highest ECs are mostly at wavelengths between 20 and 300 km at MGD, ATH, and RIK, while it is above 200 km at SGK. This shorter limit of wavelengths (20 km) may be due to the thickness of 557.7-nm airglow layer (~10 km). Thus, if the horizontal and vertical

wavelengths of the observed AGWs are comparable, their amplitude in airglow images will be suppressed. It may also correspond to the shorter limit of the horizontal wavelength of AGWs (e.g., Fritts et al., 1997). The larger limit of wavelengths (300–500 km) may be due to the limitation of the field of view of the airglow imagers. The EC peak tends to distribute around a wavelength of 100 km for all spectra in Figures 1 and 2 except for that of SGK, which shows high ECs at wavelengths longer than 100 km.

In Figure 3, the power spectra in summer are stronger than those in other seasons over ~20–100 km at RIK and SGK regardless of solar activity. This tendency can be also seen in ATH and MGD in solar active time. This tendency is possibly caused by a seasonal difference of AGW sources in the lower atmosphere. Tsuchiya et al. (2018, 2019) showed the distribution of vertical flow velocity at an altitude about 7 km, which could be the wave source in the troposphere, based upon the ERA Interim, European Centre for Medium-Range Forecasts. The upward flow in summer is stronger than in winter at MGD, RIK, and SGK. At ATH, the upward flow at the east of ATH is not much different between summer and winter. In summer the preference of propagation direction is northward (poleward) for all the stations, as shown in Figures 1 and 2. This northward propagation suggests mesospheric duct propagation of AGWs from the wave source located at south of the observation sites, as cited in section 3. Since the ducting AGWs have large vertical wavelengths, it may contribute to intensify the amplitude of AGWs in airglow intensity, because larger vertical wavelength results in less phase difference in altitudes within the airglow layer.

In Figure 4, the PSDs at 30–100 km are largest at RIK and then ATH, compared with MGD and SGK. The spectral slope in the wavelengths between 20 and 100 km is steepest at MGD ( $-3.22$ ), and then RIK ( $-3.11$ ), ATH ( $-2.77$ ), and SGK ( $-2.68$ ). The main sources of the AGWs include orography, convection, and jet and front systems (e.g., Plougonven & Zhang, 2014; Miller et al., 2015). Tropospheric convections dominate at low latitudes, while jets and fronts dominate at middle latitudes. The Joule heating in the auroral zone can be another cause of AGWs near the auroral zone (ATH [MLAT 61.1–61.7°N] and then MGD [MLAT: 51.9°N]) (e.g., Richmond, 1978). The jets and fronts and the auroral Joule heating may be the reason of the enhanced PSDs at RIK and ATH, respectively, because RIK is close to the peak location of tropospheric and mesospheric jet and ATH is closest to the auroral zone. However, we should note that the AGWs in summer in ATH mainly propagate poleward, which is opposite to that from the auroral zone.

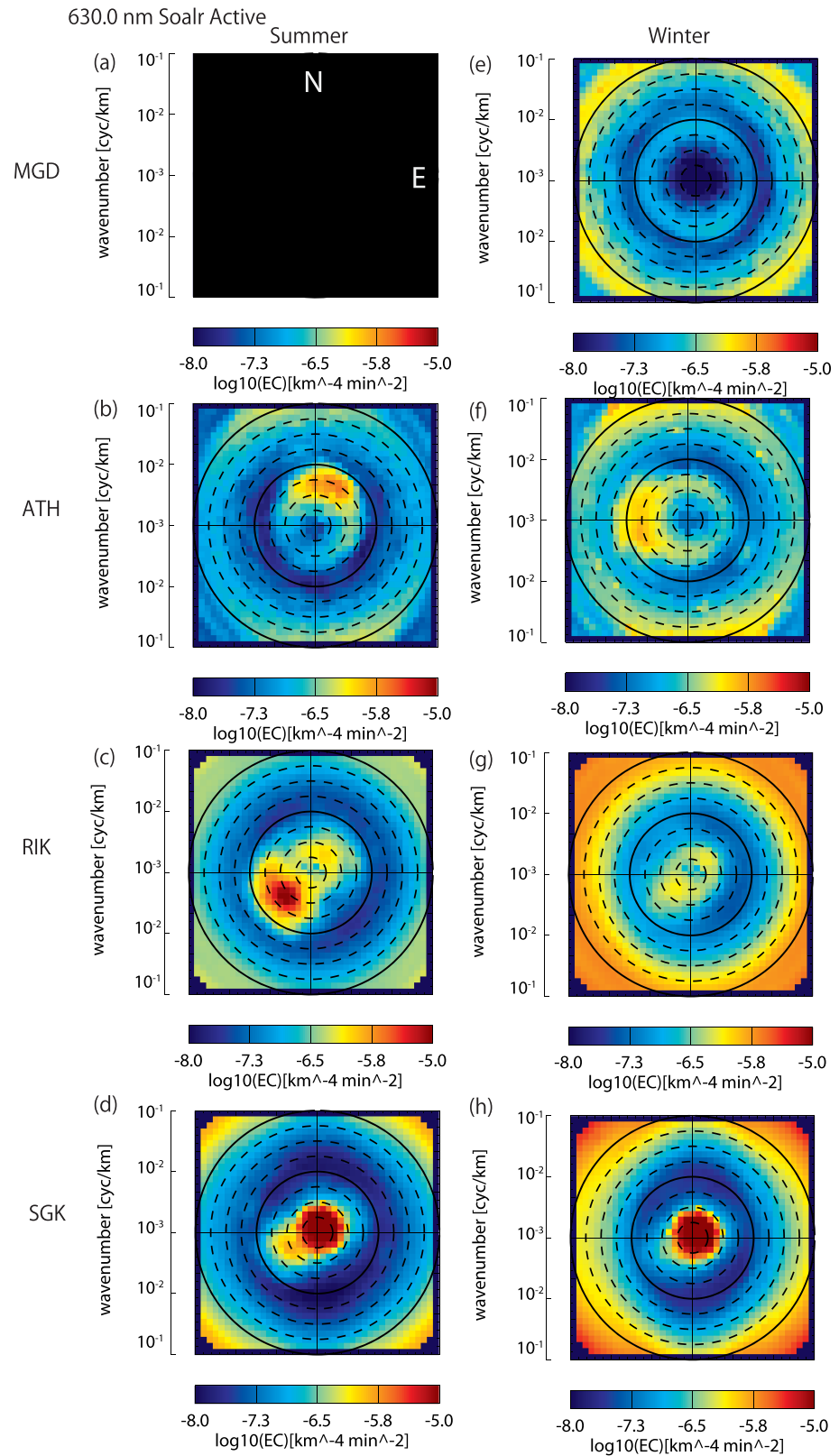


**Figure 5.** Seasonal averages of the energy content (EC) of the horizontal wavenumber of MSTIDs seen in 630.0-nm air-glow images at MGD (a and e), ATH (b and f), RIK (c and g), and SGK (d and h) in summer (a–d) and winter (e and f) in the solar active time (1999–2004 and 2011–2015).

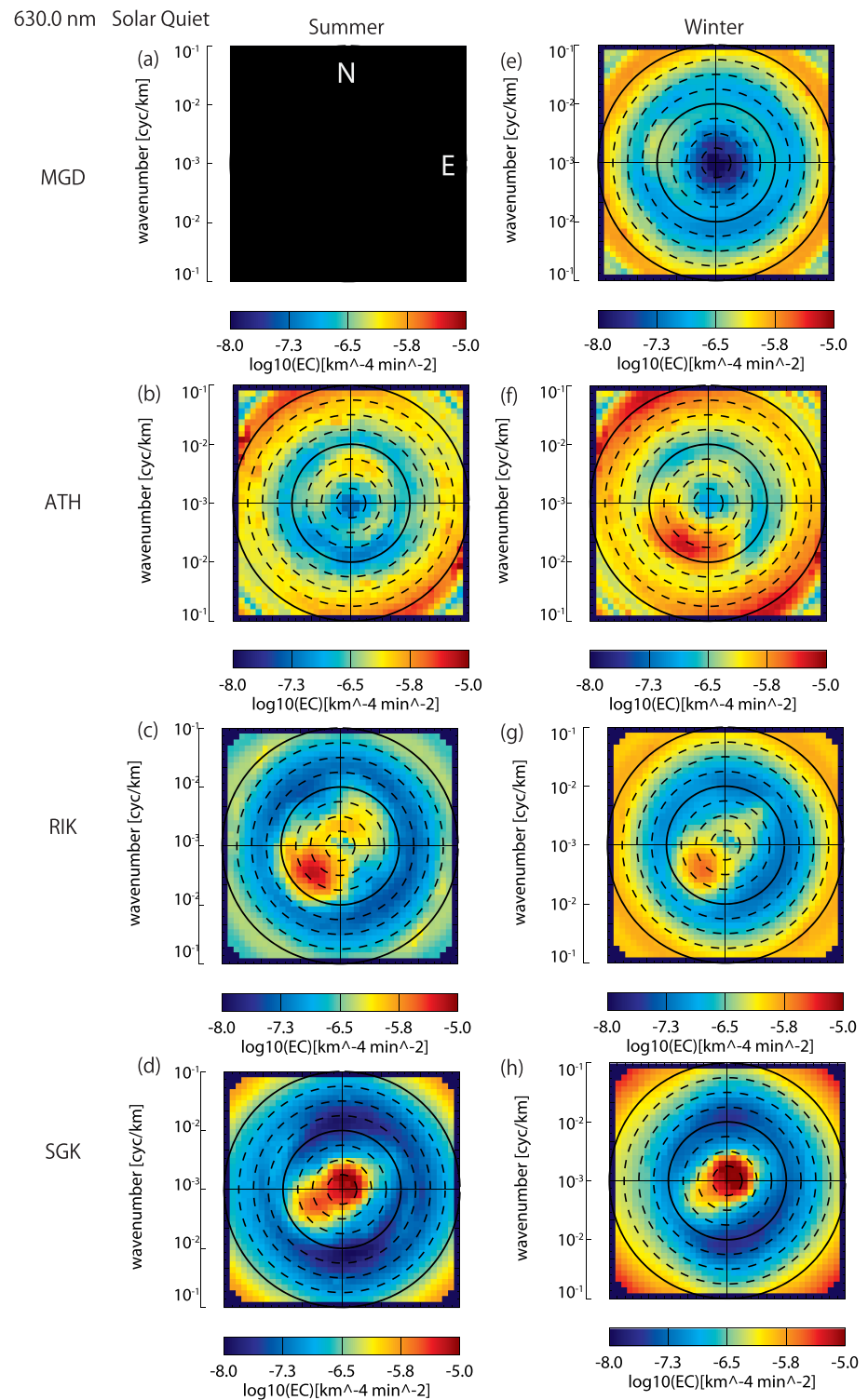


**Figure 6.** Seasonal averages of the energy content (EC) of the horizontal wavenumber of MSTIDs seen in 630.0-nm air-glow images at MGD (a and e), ATH (b and f), RIK (c and g), and SGK (d and h) in summer (a–d) and winter (e and f) in the solar quiet time (2005–2010).

**Table 3**  
Energy Content (EC), Propagation Direction, and Wavelengths of Main EC Peak and Secondary EC Peak in MSTID Spectra Shown in Figures 5 and 6

MSTID (630.0 nm)	EC in unit of ( $\text{km}^{-4} \cdot \text{min}^{-2}$ )	Solar active (Figure 5)		Solar quiet (Figure 6)	
		Summer	Winter	Summer	Winter
MGD	main EC peak	—	log <sub>10</sub> (EC): -7.0 OMNI except for E 100–200 km	—	log <sub>10</sub> (EC): -6.5 W 50–200 km
	secondary EC peak	—	—	—	—
ATH	main EC peak	log <sub>10</sub> (EC): -5.8 N-NE 100–400 km	log <sub>10</sub> (EC): -6.2 W 50–300 km	log <sub>10</sub> (EC): -6.1 N 100–400 km	log <sub>10</sub> (EC): -5.2 SW-S 50–300 km
	secondary EC peak	—	log <sub>10</sub> (EC): -6.5 OMNI except for E 200–300 km	log <sub>10</sub> (EC): -6.5 OMNI except for SW 200–300 km	log <sub>10</sub> (EC): -6.3 N 200–300 km
RIK	main EC peak	log <sub>10</sub> (EC): -5.0 SW 50–500 km	log <sub>10</sub> (EC): -6.1 SW 200–500 km	log <sub>10</sub> (EC): -5.2 SW 50–500 km	log <sub>10</sub> (EC): -5.8 SW 100–500 km
	secondary EC peak	log <sub>10</sub> (EC): -6.1 NE 200–500 km	log <sub>10</sub> (EC): -6.2 NE 300–500 km	log <sub>10</sub> (EC): -6.3 NE 100–500 km	log <sub>10</sub> (EC): -6.5 NE 100–500 km
SGK	main EC peak	log <sub>10</sub> (EC): -5.0 NE >300 km	log <sub>10</sub> (EC): -5.0 NE >300 km	log <sub>10</sub> (EC): -5.2 NE >300 km	log <sub>10</sub> (EC): -5.0 NE >300 km
	secondary EC peak	log <sub>10</sub> (EC): -6.0 SW 100–500 km	log <sub>10</sub> (EC): -6.5 SW 100–300 km	log <sub>10</sub> (EC): -5.8 SW 100–500 km	log <sub>10</sub> (EC): -6.0 SW 200–500 km

The higher spectral slope at MGD and RIK may also correspond to dominant larger scale of AGWs originated from jets and fronts rather than smaller-scale tropospheric convection.

Hecht et al. (1994) showed that the spectral slope of horizontal wavenumber is between  $-2.5$  and  $-3$  by using airglow images at Illinois and Puerto Rico. These values are comparable to the present result. Gardner et al. (1993) and Gardner (1994) presented two spectral models of AGWs which assume that the frequency and vertical wavenumber spectra are separable and not separable. These two models show that the slope is  $-4$  (separable model) and  $-3$  (nonseparable model). The slope given by the nonseparable model is close to the present results.

## 5. Results From the 630.0-nm Airglow Images

Figures 5 and 6 show seasonal averages of the distribution of EC ( $\text{EC} = \text{PSD} * \text{k}^2$ ) of MSTIDs seen in 630.0-nm airglow images for the horizontal wavenumber space in the solar active time and quiet time, respectively, at MGD (a and e), ATH (b and f), RIK (c and g), and SGK (d and h) in summer (a–d) and winter (e and f). Table 3 summarizes the EC, propagation direction, and wavelengths for the main EC peak and secondary EC peak in MSTID spectra in Figures 5 and 6.

In summer, clear contrast can be seen between ATH and RIK/SGK, the former is northward at wavelengths of 100–400 km, while the latter is southwestward at 50–500 km. The northward MSTID at ATH in summer was reported by Shiokawa et al. (2013) as a signature of AGWs, while the southwestward preference of MSTIDs at middle latitude like RIK and SGK has been reported by many references (e.g., Garcia et al., 2000; Martinis et al., 2010; Otsuka et al., 2013; Shiokawa et al., 2003). It should be noted that the main EC peak at SGK was northeastward at wavelengths of more than 300 km in both summer and winter. The secondary peak at RIK is also northeastward at 100–500 km. These southwestward and northeastward preferences of MSTIDs are consistent with those expected from Perkins instability (Perkins, 1973), because these directions are perpendicular to the phase surface direction expected from the instability.

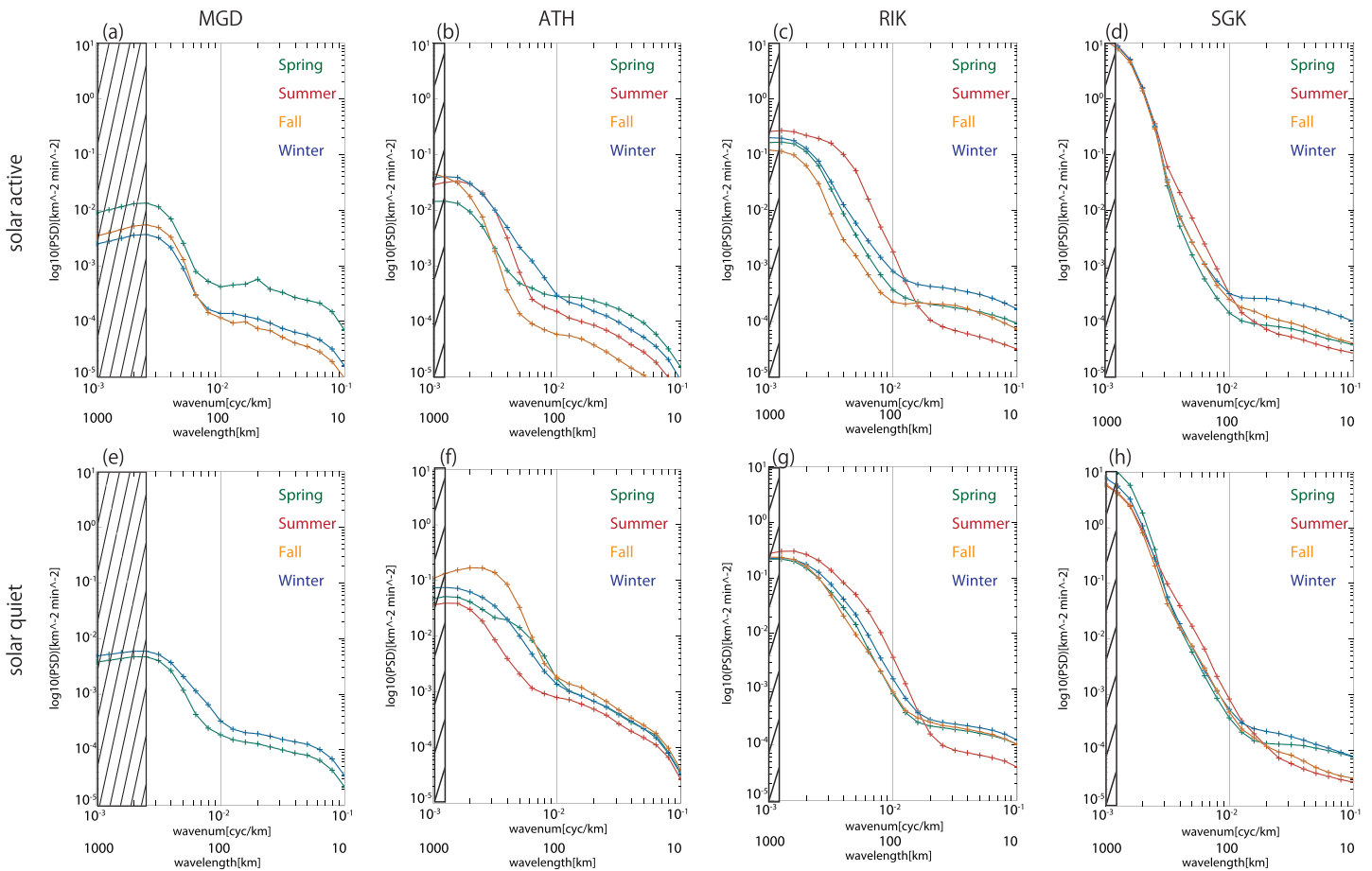


**Figure 7.** Seasonal averages of the horizontal wavenumber spectra of MSTIDs in 630.0-nm airglow images at MGD (a and e), ATH (b and f), RIK (c and g), and SGK (d and h) in the solar active (a–d) and quiet (e–h) time. The line colors show the seasons as spring (green), summer (red), fall (orange), and winter (blue). The hatched areas represent outside the data coverage (800 or 400 km).

In winter at MGD, the propagation direction of MSTIDs over 50–200 km is westward in solar quiet time, while it is very weak and omnidirectional except for eastward in solar active time. The EC at MGD is basically very small compared with other stations. The propagation direction of MSTIDs over 50–500 km in winter is westward at ATH in solar active time and southwestward in solar quiet time. These directions at ATH are also consistent with those expected from the Perkins instability.

Figure 7 shows the seasonal averages of the horizontal wavenumber spectra of MSTIDs at MGD (a and e), ATH (b and f), RIK (c and g), and SGK (d and h) in the solar active time (a–d) and the solar quiet time (e–h). The line colors show the seasons as spring (green), summer (red), fall (orange), and winter (blue). The power spectrum in summer is systematically stronger than those in other seasons over 100–500 and 100–300 km at RIK and SGK, respectively, for both solar active and quiet times. This tendency cannot be seen in ATH. The airglow image data in summer are not available at MGD, because it is located at high latitudes.

Figure 8 shows the horizontal wavenumber spectra of MSTIDs in solar active time (red) and solar quiet time (blue) at MGD (a and e), ATH (b and f), RIK (c and g), and SGK (d and h) in summer (a–d) and winter (e–h). The power spectra in solar quiet time are stronger than those in solar active time in both summer and winter at wavelengths of several tens to hundreds of kilometers. As exceptions, the power spectrum in active time is comparable or stronger than in quiet time at wavelengths more than ~400 km at SGK (both seasons), and ATH and RIK (in summer). This large wavelength range is close to the limit of the 3-D FFT due to the limitation of the image size (800 × 800 km).

Figure 9 shows comparison of the horizontal wavenumber spectra of MSTIDs in 630.0-nm airglow images at MGD (green), ATH (red), RIK (blue), and SGK (orange) averaged over whole analysis periods. The power

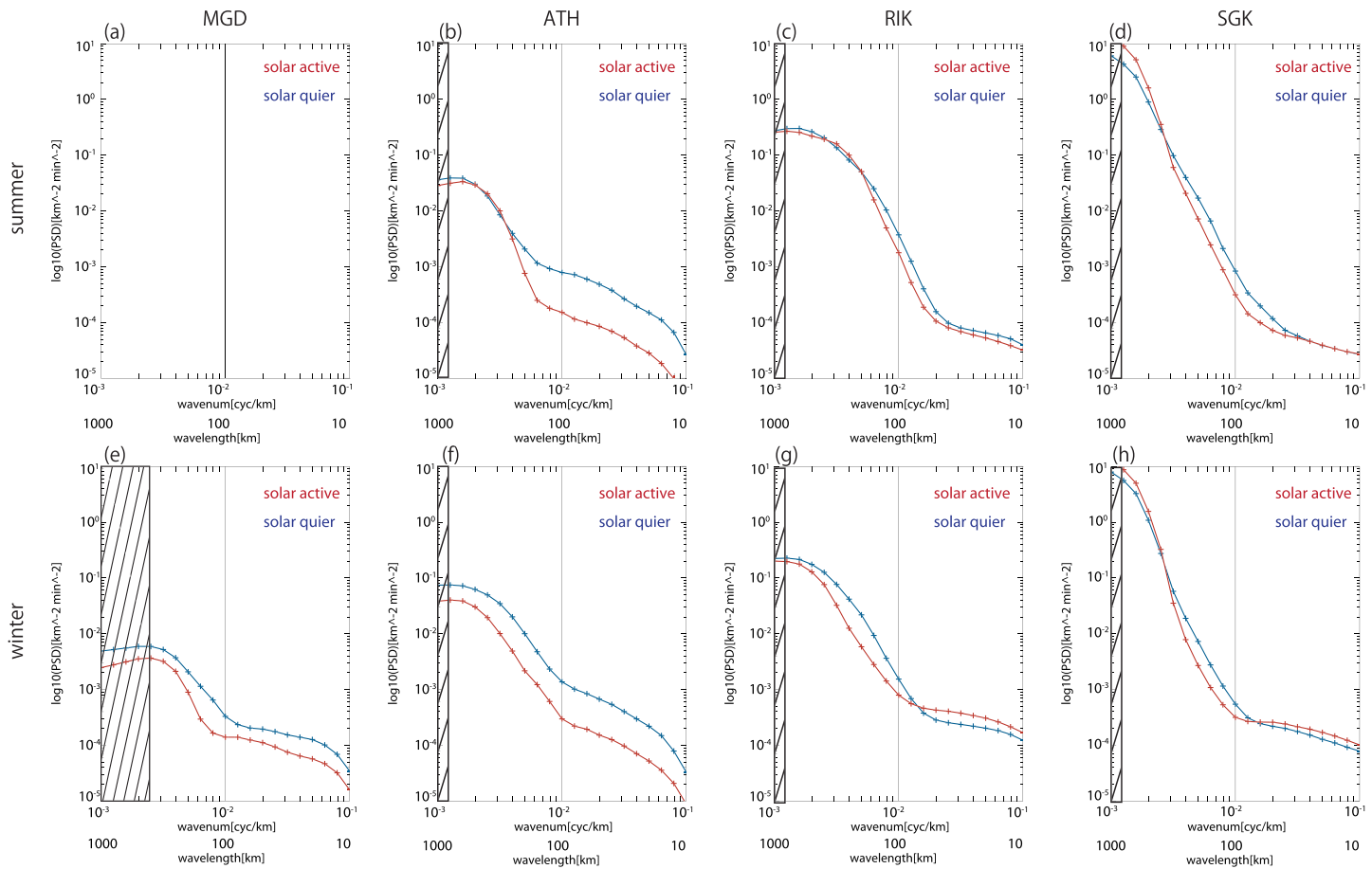


**Figure 8.** Horizontal wavenumber spectra of MSTIDs in 630.0-nm airglow images in solar active (red) and quiet (blue) times at MGD (a and e), ATH (b and f), RIK (c and g), and SGK (d and h) in summer (a–d) and winter (e–h).

spectra at RIK is strongest at wavelengths of 100–300 km and then ATH, SGK, and MGD. The slope of the power spectrum between 100 and 250 km at MGD, ATH, RIK, and SGK is  $-2.77$ ,  $-3.68$ ,  $-3.88$ , and  $-4.07$ , respectively. The spectral slope clearly decreases with increasing latitudes.

## 6. Discussion of the 630.0-nm Results

The power spectrum in solar quiet time is stronger than in solar active time at all four stations. This tendency has been reported by Takeo et al. (2017) and Tsuchiya et al. (2018, 2019) as yearly variation plots of the PSDs of MSTIDs, and can be explained by the linear growth rate of the Perkins instability (Perkins, 1973). The linear growth rate of the Perkins instability is inversely proportional to the plasma density-weighted field-line-integrated ion-neutral collision frequency and the scale height of the neutral atmosphere. The ion-neutral collision frequency and the scale height increase as the solar activity increases. Thus, the growth rate of Perkins instability is expected to have negative correlation with the solar activity.

The AGW amplitude at a fixed altitude increases during solar quiet interval due to decreasing density. This may be also consistent with the negative correlation between MSTID power and solar activity. However, AGWs tend to be more dissipated at lower altitudes during solar quiet interval due to increasing kinematic viscosity (e.g., Vadas et al., 2014). This may also allow more generation of secondary AGWs in the thermosphere, as a source of the MSTIDs.

The power spectra in summer are stronger than that in other seasons at RIK and SGK. This tendency can be also explained by considering the coupling between sporadic *E* (*Es*) and *F* layer (e.g., Cosgrove & Tsunoda, 2004; Tsunoda & Cosgrove, 2001). Yokoyama et al. (2009) indicated the coupling between the Perkins instability in *F* region and *Es* layer instability as the cause of the MSTIDs, because the growth rate of

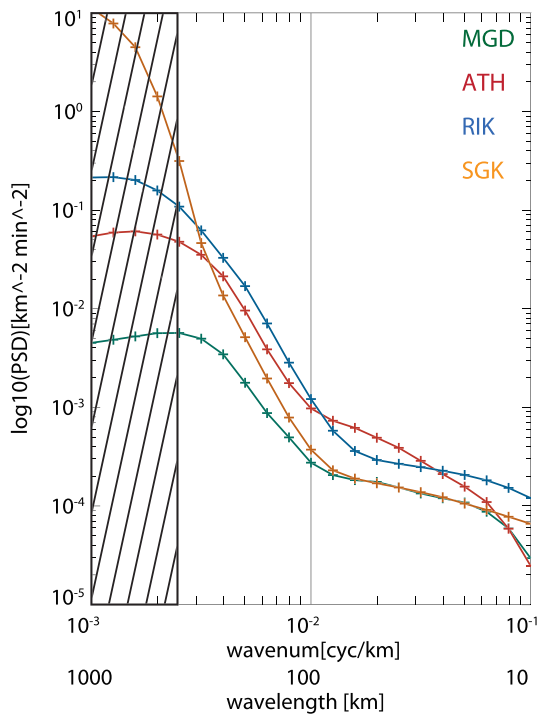


**Figure 9.** Horizontal wavenumber spectra of MSTIDs in 630.0-nm airglow images at MGD (green), ATH (red), RIK (blue), and SGK (orange) averaged over whole analysis periods.

Perkins instability in *F* region is generally rather small. Narayanan et al. (2018) indicated by using geomagnetic conjugate airglow imagers, ionosondes, and Fabry-Perot interferometers in Japan and Australia that the existence of *Es* layer on at least one hemisphere of MSTID-connected geomagnetic field line is sufficient for the generation of MSTIDs. Thus, the seasonal variation of the *Es* layer occurrence is important to consider the seasonal variation of the MSTIDs occurrence. The *Es* layer occurrence rate is high in Japan (Northern Hemisphere) around the June solstice and in Australia (Southern Hemisphere) around the December solstice, and the plasma density of the *Es* layer in Japan around the June solstice is higher than in Australia around the December solstice (e.g., Taguchi & Shibata, 1961). This seasonal variation of the *Es* layer occurrence in Japan is consistent with the results obtained from RIK and SGK. The second strongest spectrum in winter at RIK in Figures 7c and 7g may correspond to the peak of the *Es* layer occurrence in Australia. However, this tendency is not clearly seen at SGK.

In Figure 9, the power spectra at RIK are strongest, followed by ATH, SGK, and MGD at wavelengths of ~100–300 km. This order of RIK (strongest) and then ATH is the same to that of AGWs in the mesopause region in Figure 4. Thus, the AGWs from the mesopause region may contribute to produce this difference of power spectra of MSTIDs among stations, though the focused wavelengths are different between Figure 4 (~30–100 km) and Figure 9 (~100–300 km). The AGWs can be a seed of the instability to cause MSTIDs by providing initial perturbation, and/or can directly cause MSTIDs. Otsuka et al. (2013) showed that the occurrence rate of nighttime MSTIDs observed by Global Positioning System observa-

tions is lower at high latitudes than at low latitudes in Europe. They discuss that the steeper inclination of geomagnetic field at higher latitudes may cause the lower occurrence of MSTIDs caused by Perkins instability, because the amplitude of total electron content variation depends on cosine of magnetic field inclination. However, the geomagnetic field intensity, which determines the  $E \times B$  drift velocity associated with the polarization electric field in the Perkins instability, increases with increasing latitudes. Thus, two competing effects (inclination and magnetic field intensity) may work to create the latitudinal variation of power spectra for the Perkins instability. The order of magnetic inclination angles and magnetic field intensity are from high to low, ATH (76°, 50,726 nT), MGD (72°, 50,023 nT), RIK (58°, 44,243 nT), and SGK (49°, 41,645 nT) in 2017 at an altitude of 250 km according to the International Reference Geomagnetic Field. This order is, however, different from that of PSD (RIK, ATH, SGK, and MGD) in Figure 9. The difference of magnetic field intensity between ATH and MGD is only ~1%, which is not likely able to explain the large PSD difference in Figure 9 through the  $E \times B$  drift velocity.

The spectral slope at 100–250 km decreases with increasing latitudes from SGK to MGD. This may also correspond to the increase of inclination of magnetic field from low to high latitudes. Although the Perkins instability does not predict horizontal scale sizes, the smaller inclination may cause larger-scale travelling ionospheric disturbance in horizontal wavelengths, because the polarization electric field by the Perkins instability develops perpendicular to the magnetic field line.

## 7. Correlation Between AGWs and MSTIDs

In order to investigate the possibility that the AGWs in the mesopause region are a cause of the MSTIDs in the thermosphere, we check the correlation of wave power between AGWs in 557.7-nm airglow images and MSTIDs in 630.0-nm airglow images. Figure 10 shows the correlation between the nightly averaged 557.7- and 630.0-nm wave power at (a) MGD, (b) ATH, (c) RIK, and (d) SGK. The nightly averaged power observed on the same night were plotted. The power spectra of 557.7- and 630.0-nm airglow images were integrated over 10–100 and 100–250 km, respectively, in all directions. We did not take the same range of integration for these two airglow images, because of the limitation of the field of view (200 × 200 km or 400 × 400

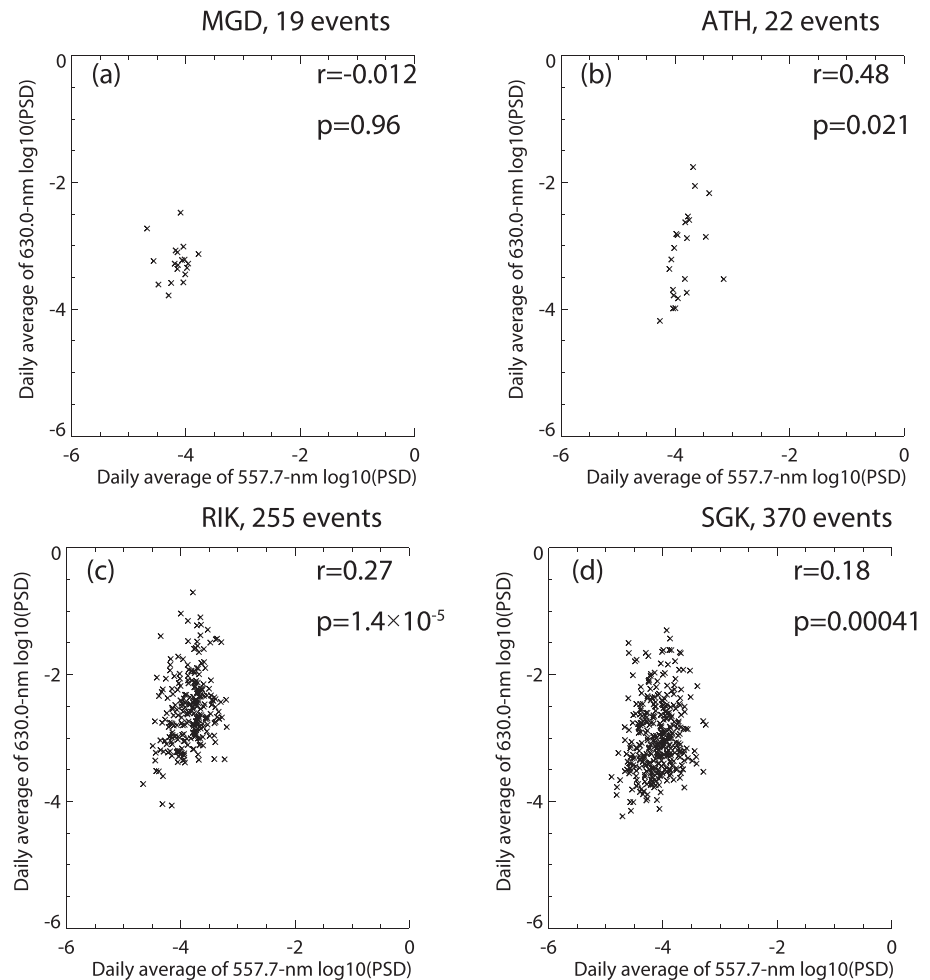


**Figure 10.** Correlation between the nightly averaged 557.7- and 630.0-nm power spectra at (a) MGD, (b) ATH, (c) RIK, and (d) SGK. The value  $r$  is the correlation coefficient between these spectra, while  $p$  is the  $p$  value, which indicates the possibility of invalidity of the calculated correlation coefficient; that is, the correlation coefficient with smaller  $p$  value is more reliable.

km) of images for the 557.7-nm airglow and because of the vertical thickness of 630.0-nm airglow, which is  $\sim 100$  km and tends to smear out waves with scale sizes less than  $\sim 100$  km. The value  $r$  is the correlation coefficient between these integrated wave powers, while  $p$  is the  $p$  value, which indicates the possibility of invalidity of the calculated correlation coefficient and is a function of the number of data points. Namely, the correlation coefficient with smaller  $p$  value is more reliable. The correlations between the spectra of waves in 557.7- and 630.0-nm airglow images are  $-0.012$ ,  $0.48$ ,  $0.31$ , and  $0.18$  at MGD, ATH, RIK, and SGK, respectively. We can see weak positive correlation between the nightly averaged wave power in 557.7- and 630.0-nm airglow images at ATH, RIK, and SGK.

This weak positive correlation suggests that the MSTIDs in the thermosphere may be partially generated by the AGWs from the mesopause region. However, the propagation directions of AGWs in 557.7-nm images and MSTIDs in 630.0-nm images are usually very different (e.g., Tsuchiya et al., 2018, 2019). The MSTIDs may be caused by secondary waves, which is generated by dissipation of the primary waves in the lower thermosphere (e.g., Vadas, 2007). The propagation direction of secondary waves can be different from the propagation direction of primary AGWs. The AGWs can also provide initial perturbation of the Perkins and  $E$ - $F$  coupling instabilities, possibly causing the observed weak correlation in Figure 10. Previous studies suggest that AGWs are important in the daytime MSTIDs (e.g., Miyoshi et al., 2018), while nighttime electrodynamic instabilities play major role for nighttime MSTIDs (e.g., Makela & Otsuka, 2012) at middle and low latitudes.

**Table 4**  
Seasonal Variation of the Correlation Between the Nightly Averaged 557.7-nm and 630.0-nm Power Spectra at MGD, ATH, RIK, and SGK

	Magadan		Athabasca		Rikubetsu		Shigaraki	
	number of events	correlation coefficient						
spring	6	0.41	7	0.68	47	0.27	85	0.22
summer			4	-0.45	35	0.20	62	-0.15
fall	3	0.72	5	0.90	22	0.39	55	0.02
winter	10	-0.23	6	0.71	151	0.17	168	0.26

Table 4 shows the seasonal variation of the correlation coefficients between the nightly averaged 557.7- and 630.0-nm wave powers at MGD, ATH, RIK, and SGK. The correlation coefficients in summer are smaller than those in other seasons at ATH, RIK, and SGK. This may be because the occurrence rate of MSTIDs caused by the Perkins instability with coupling between *Es* and *F* layer is highest in summer, because the occurrence rate of *Es* layer is highest in summer, as discussed in section 6. The high occurrence of Perkins-type MSTIDs in summer may mask the effect of thermospheric gravity waves, being another cause of waves in 630.0-nm airglow images, and reduce the correlation coefficient in Table 4 in summer.

## 8. Summary

We have applied the three-dimensional FFT spectral analysis technique by Matsuda et al. (2014) to the 557.7- and 630.0-nm airglow images over 10 years at SGK (34.8°N, 136.1°E, MLAT: 25.4°N) and RIK (43.5°N, 143.8°E, MLAT: 34.7°N), Japan, ATH, Canada (54.7°N, 246.7°E, MLAT: 61.7°N and 54.6°N, 246.3°E, MLAT: 61.1°N), and MGD, Russia (60.1°N, 150.7°E, MLAT: 51.9°N) and have obtained their horizontal wavenumber spectra. We examined similarities and differences of these wavenumber spectra to see their dependence on the location, season, and solar activity.

We obtained the following conclusions based on the spectral analysis of AGWs in 557.7-nm airglow images.

1. The highest EC of the spectra are mostly at wavelengths between 20 and 300 km at MGD, ATH, and RIK, while it is above 200 km at SGK. The EC peak tends to distribute around a wavelength of 100 km for all spectra except for that of SGK which shows high ECs at wavelengths longer than 100 km.
2. The power spectra in summer are stronger than those in other seasons over ~20–100 km at RIK and SGK regardless of solar activity. This tendency can be also seen in ATH and MGD in solar active time. This tendency is possibly caused by seasonal difference of AGW sources in the lower atmosphere.
3. The largest PSD is obtained at RIK at 30–100 km and then ATH, compared with MGD and SGK. The slopes of the wavenumber spectra at wavelengths between 20 and 100 km at MGD, ATH, RIK, and SGK were -3.22, -2.77, -3.11, and -2.68, respectively. We suggest that these differences of the PSDs and their slopes may originate from difference in wavelength distribution of AGW sources at different stations.

We also obtained the following conclusions based on the spectral analysis of MSTIDs in 630.0-nm airglow images.

1. In summer, clear contrast can be seen between ATH and RIK/SGK, the former is northward at wavelengths of 100–400 km, while the latter is southwestward at 50–500 km. In winter at ATH, the propagation direction over 50–500 km is westward in solar active time and southwestward in solar quiet time. The main EC peak at SGK was northeastward at wavelengths of more than 300 km in both summer and winter. The secondary peak at RIK is also northeastward at 100–500 km in both summer and winter. These southwestward and northeastward preferences of MSTIDs is consistent with those expected from Perkins instability, while northward wave in ATH in summer can be AGWs. The EC at MGD is basically very small compared with other stations.
2. The MSTID powers in summer are systematically stronger than those in other seasons over 100–500 and 100–300 km at RIK and SGK, respectively, for both solar active and quiet periods. Such tendency cannot be seen in ATH. This high MSTID power in summer can be explained by considering the Perkins

- instability with coupling between sporadic *E* and *F* layers. The stronger *Es* layer over Japan in summer reported in previous literatures is also consistent with this stronger MSTID power at RIK and SGK.
3. The MSTID powers in solar quiet time are stronger than those in solar active time at all four stations at wavelengths of several tens to hundreds of kilometers. This tendency is also consistent with the solar activity dependence expected from the linear growth rate of the Perkins instability. We also point out that the AGW amplitude at a fixed altitude increases during solar quiet interval due to decreasing density.
  4. The spectral slopes at horizontal wavelengths between 100 and 250 km at MGD, ATH, RIK, and SGK are  $-2.77$ ,  $-3.68$ ,  $-3.88$ , and  $-4.07$ , respectively. These spectral slopes decrease with increasing latitudes. This tendency can be understood by the increase of magnetic inclination with latitudes and the polarization electric field of the Perkins instability, which develops perpendicular to the magnetic field line.

Finally, we obtained the following conclusions based on the correlation between the spectra of AGWs and MSTIDs in 557.7- and 630.0-nm airglow images, respectively.

1. The correlations between the wave spectra of 557.7- and 630.0-nm airglow images are  $-0.012$ ,  $0.48$ ,  $0.31$ , and  $0.18$  at MGD, ATH, RIK, and SGK, respectively. The weak positive correlation at ATH, RIK, and SGK may indicate that the MSTIDs in the thermosphere may be partially generated by the AGWs from the mesopause region. The AGWs can also provide initial perturbation of the Perkins and *E-F* coupling instabilities, possibly causing this weak positive correlation.
2. The correlation coefficient in summer is smaller than those in other seasons at ATH, RIK, and SGK. This may be because the occurrence rate of MSTIDs caused by the Perkins instability with coupling between *Es* and *F* layer is highest in summer, masking the effect of AGWs in the thermosphere to cause the MSTIDs.

#### Acknowledgments

We would like to thank T. Katoh, M. Satoh, Y. Katoh, Y. Hamaguchi, Y. Yamamoto, T. Adachi, and N. Yokozeki of the Solar-Terrestrial Environment Laboratory/Institute for Space-Earth Environmental Research (ISEE), Nagoya University, for their support and help with the airglow imaging observations. The all-sky airglow images used in this study are available at ISEE, Nagoya University from the website ([https://ergsc.isee.nagoya-u.ac.jp/data\\_info/ground.shtml.en](https://ergsc.isee.nagoya-u.ac.jp/data_info/ground.shtml.en)). This research was supported by the JSPS Core-to-Core Program, B. Asia-Africa Science Platforms, and JSPS KAKENHI Grants (JP 15H05815 and JP 16H06286).

#### References

- Amorim, D. C. M., Pimenta, A. A., Bittencourt, J. A., & Fagundes, P. R. (2001). Long-term study of medium-scale traveling ionospheric disturbances using OI 630 nm all-sky imaging and ionosonde over Brazilian low latitudes. *Journal of Geophysical Research*, *116*(A6), A06312. <https://doi.org/10.1029/2010JA016090>
- Azeem, I., Yue, J., Hoffmann, L., Miller, S. D., Straka, W. C., & Crowley, G. (2015). Multisensor profiling of a concentric gravity wave event propagating from the troposphere to the ionosphere. *Geophysical Research Letters*, *42*, 7874–7880. <https://doi.org/10.1002/2015GL065903>
- Coble, M., Papen, G. C., & Gardner, C. S. (1998). Computing two-dimensional unambiguous horizontal wavenumber spectra from OH airglow images. *IEEE Transactions on Geoscience and Remote Sensing*, *36*(2), 368–382. <https://doi.org/10.1109/36.662723>
- Cosgrove, R. B., & Tsunoda, R. T. (2004). Instability of the *E-F* coupled nighttime midlatitude ionosphere. *Journal of Geophysical Research*, *109*, A04305. <https://doi.org/10.1029/2003JA010243>
- Davies, K. (1990). *Ionospheric Radio*. London: Peter Peregrinus.
- Ejiri, M. K., Shiokawa, K., Ogawa, T., Igarashi, K., Nakamura, T., & Tsuda, T. (2003). Statistical study of short-period gravity waves in OH and OI nightglow images at two separated sites. *Journal of Geophysical Research*, *108*(D21), 4679. <https://doi.org/10.1029/2002JD002795>
- Fritts, D. C., & Alexander, M. J. (2003). Gravity wave dynamics and effects in the middle atmosphere. *Reviews of Geophysics*, *41*(1), 1003. <https://doi.org/10.1029/2001RG000106>
- Fritts, D. C., Isler, J. R., Hecht, J. H., Walterscheid, R. L., & Andreassen, O. (1997). Wave breaking signatures in sodium densities and OH nightglow: 2. Simulation of wave and instability structures. *Journal of Geophysical Research*, *102*(D6), 6669–6684. <https://doi.org/10.1029/96JD01902>
- Garcia, F. J., Kelley, M. C., Makela, J. J., & Huang, C.-S. (2000). Airglow observations of mesoscale low-velocity traveling ionospheric disturbances at midlatitudes. *Journal of Geophysical Research*, *105*(A8), 18,407–18,415. <https://doi.org/10.1029/1999JA000305>
- Gardner, C. S. (1994). Diffusive filtering theory of gravity wave spectra in the atmosphere. *Journal of Geophysical Research*, *99*(D10), 20,601–20,622. <https://doi.org/10.1029/94JD00819>
- Gardner, C. S., Hostetler, C. A., & Franke, S. J. (1993). Gravity wave models for the horizontal wave number spectra of atmospheric velocity and density fluctuations. *Journal of Geophysical Research*, *98*(D1), 1035–1049. <https://doi.org/10.1029/92JD02051>
- Hecht, J. H., Walterscheid, R. L., & Ross, M. N. (1994). First measurements of the two-dimensional horizontal wave number spectrum from CCD images of the nightglow. *Journal of Geophysical Research*, *99*(A6), 11,449–11,460. <https://doi.org/10.1029/94JA00584>
- Hunsucker, R. D. (1982). Atmospheric gravity waves generated in the high latitude ionosphere: A review. *Reviews of Geophysics*, *20*(2), 293–315. <https://doi.org/10.1029/RG020i002p00293>
- Makela, J. J., & Kelley, M. C. (2003). Using the 630.0-nm nightglow emission as a surrogate for the ionospheric Pedersen conductivity. *Journal of Geophysical Research*, *108*(A6), 1253. <https://doi.org/10.1029/2003JA009894>
- Makela, J. J., & Otsuka, Y. (2012). Overview of nighttime ionospheric instabilities at low- and mid-latitudes: Coupling aspects resulting in structuring at the mesoscale. *Space Science Reviews*, *168*, 419–440. <https://doi.org/10.1007/s11214-011-9816-6>
- Martinis, C., Baumgardner, J., Wroten, J., & Mendillo, M. (2010). Seasonal dependence of MSTIDs obtained from 630.0 nm airglow imaging at Arecibo. *Geophysical Research Letters*, *37*, L11103. <https://doi.org/10.1029/2010GL043569>
- Matsuda, T. S., Nakamura, T., Ejiri, M. K., Tsutsumi, M., & Shiokawa, K. (2014). New statistical analysis of the horizontal phase velocity distribution of gravity waves observed by airglow imaging. *Journal of Geophysical Research: Atmospheres*, *119*, 9707–9718. <https://doi.org/10.1002/2014JD021543>
- Matsuno, T. (1982). A quasi one-dimensional model of the middle atmosphere circulation interacting with internal gravity waves. *Journal of the Meteorological Society of Japan Series II*, *60*(1), 215–226. <https://doi.org/10.2151/jmsj1965.60.1-215>

- Miller, S. D., Straka, W. C., Yue, J., Smith, S. M., Alexander, M. J., Hoffmann, L., et al. (2015). Upper atmospheric gravity wave details revealed in nightglow satellite imagery. *Proceedings of the National Academy of Sciences*, *112*(49), E6728–E6735. <https://doi.org/10.1073/pnas.1508084112>
- Miyoshi, Y., Jin, H., Fujiwara, H., and Shinagawa, H. (2018). Numerical study of traveling ionospheric disturbances generated by an upward propagating gravity wave. *Journal of Geophysical Research: Space Physics*, *123*, 2141–2155. <https://doi.org/10.1002/2017JA025110>
- Nakamura, T., Higashikawa, A., Tsuda, T., & Matsushita, Y. (1999). Seasonal variations of gravity wave structures in OH airglow with a CCD imager at Shigaraki. *Earth, Planets and Space*, *51*(7-8), 897–906. <https://doi.org/10.1186/BF03353248>
- Narayanan, L., Shiokawa, K., Otsuka, Y., & Saito, S. (2014). Airglow observations of nighttime medium-scale traveling ionospheric disturbances from Yonaguni: Statistical characteristics and low-latitude limit. *Journal of Geophysical Research: Space Physics*, *119*, 9268–9282. <https://doi.org/10.1002/2014JA020368>
- Narayanan, V. L., Shiokawa, K., Otsuka, Y., & Neudegg, D. (2018). On the role of thermospheric winds and sporadic E layers in the formation and evolution of electrified MSTIDs in geomagnetic conjugate regions. *Journal of Geophysical Research: Space Physics*, *123*, 6957–6980. <https://doi.org/10.1029/2018JA025261>
- Otsuka, Y., Shiokawa, K., Ogawa, T., & Wilkinson, P. (2004). Geomagnetic conjugate observations of medium-scale traveling ionospheric disturbances at midlatitude using all sky airglow imagers. *Geophysical Research Letters*, *31*, L15803. <https://doi.org/10.1029/2004GL020262>
- Otsuka, Y., Suzuki, K., Nakagawa, S., Nishioka, M., Shiokawa, K., & Tsugawa, T. (2013). GPS observations of medium-scale traveling ionospheric disturbances over Europe. *Annales de Geophysique*, *31*, 163–172. <https://doi.org/10.5194/angeo-31-163-2013>
- Perkins, F. (1973). Spread F and ionospheric currents. *Journal of Geophysical Research*, *78*(1), 216–226. <https://doi.org/10.1029/JA078i001p00218>
- Plougonven, R., & Zhang, F. (2014). Internal gravity waves from atmospheric jets and fronts. *Reviews of Geophysics*, *52*, 33–76. <https://doi.org/10.1002/2012RG000419>
- Richmond, A. D. (1978). Gravity wave generation, propagation, and dissipation in the thermosphere. *Journal of Geophysical Research*, *83*(A9), 4131–4145. <https://doi.org/10.1029/JA083iA09p04131>
- Shiokawa, K., Kato, Y., Hamaguchi, Y., Yamamoto, Y., Adachi, T., Ozaki, M., et al. (2017). Ground-based instruments of the PWING project to investigate dynamics of the inner magnetosphere at subauroral latitudes as a part of the ERG-ground coordinated observation network. *Earth, Planets and Space*, *69*, 160. <https://doi.org/10.1186/s40623-017-0745-9>
- Shiokawa, K., Kato, Y., Satoh, M., Ejiri, M. K., Ogawa, T., Nakamura, T., et al. (1999). Development of Optical Mesosphere Thermosphere Imagers 482 (OMTI). *Earth, Planets and Space*, *51*(7), 887–896. <https://doi.org/10.1186/BF03353247>
- Shiokawa, K., Mori, M., Otsuka, Y., Oyama, S., Nozawa, S., Suzuki, S., & Connors, M. (2013). Observation of nighttime medium-scale travelling ionospheric disturbances by two 630-nm airglow imagers near the auroral zone. *Journal of Atmospheric and Solar - Terrestrial Physics*, *103*, 184–194. <https://doi.org/10.1016/j.jastp.2013.03.024>
- Shiokawa, K., Otsuka, Y., Ihara, C., Ogawa, T., & Rich, F. J. (2003). Ground and satellite observations of nighttime medium-scale traveling ionospheric disturbance at midlatitude. *Journal of Geophysical Research*, *108*(A4), 1145. <https://doi.org/10.1029/2002JA009639>
- Shiokawa, K., Otsuka, Y., & Ogawa, T. (2009). Propagation characteristics of nighttime mesospheric and thermospheric waves observed by optical mesosphere thermosphere imagers at middle and low latitudes. *Earth, Planets and Space*, *61*(4), 479–491. <https://doi.org/10.1186/BF03353165>
- Suzuki, S., Shiokawa, K., Otsuka, Y., Kawamura, S., & Murayama, Y. (2013). Evidence of gravity wave ducting in the mesopause region from airglow network observations. *Geophysical Research Letters*, *40*, 601–605. <https://doi.org/10.1029/2012GL054605>
- Suzuki, S., Shiokawa, K., Otsuka, Y., Ogawa, T., & Wilkinson, P. (2004). Statistical characteristics of gravity waves observed by an all-sky imager at Darwin, Australia. *Journal of Geophysical Research*, *109*, D20S07. <https://doi.org/10.1029/2003JD004336>
- Taguchi, S., & Shibata, H. (1961). World maps of foEs. *Journal of the Radio Research Laboratories*, *8*, 355–386.
- Takeo, D., Shiokawa, K., Fujinami, H., Otsuka, Y., Matsuda, T. S., Ejiri, M. K., et al. (2017). Sixteen year variation of horizontal phase velocity and propagation direction of mesospheric and thermospheric waves in airglow images at Shigaraki, Japan. *Journal of Geophysical Research: Space Physics*, *122*, <https://doi.org/10.1002/2017JA023919>
- Taylor, M. J., & Hapgood, M. A. (1988). Identification of a thunderstorm as a source of short period gravity waves in the upper atmospheric nightglow emissions. *Planetary and Space Science*, *36*(10), 975–985. [https://doi.org/10.1016/0032-0633\(88\)90035-9](https://doi.org/10.1016/0032-0633(88)90035-9)
- Taylor, M. J., Jahn, J.-M., Fukao, S., & Saito, A. (1998). Possible evidence of gravity wave coupling into the mid-latitude F region ionosphere during the SEEK campaign. *Geophysical Research Letters*, *25*(11), 1801–1804. <https://doi.org/10.1029/97GL03448>
- Tsuchiya, S., Shiokawa, K., Fujinami, H., Otsuka, Y., Nakamura, T., Connors, M., et al. (2019). Statistical analysis of the phase velocity distributions of mesospheric and ionospheric waves based on airglow images collected over 10 years: Comparison of Magadan, Russia, and Athabasca, Canada. *Journal of Geophysical Research: Space Physics*, *124*, 8110–8124. <https://doi.org/10.1029/2019JA026783>
- Tsuchiya, S., Shiokawa, K., Fujinami, H., Otsuka, Y., Nakamura, T., & Yamamoto, M. (2018). Statistical analysis of the phase velocity distribution of mesospheric and ionospheric waves observed in airglow images over a 16-year period: Comparison between Rikubetsu and Shigaraki, Japan. *Journal of Geophysical Research: Space Physics*, *123*, 6930–6947. <https://doi.org/10.1029/2018JA025585>
- Tsugawa, T., Nishioka, M., Ishii, M., Hozumi, K., Saito, S., Shinbori, A., et al. (2018). Total electron content observations by dense regional and worldwide international networks of GNSS. *Journal of Disaster Research*, *13*(3), 535–545. <https://doi.org/10.20965/jdr.2018.p0535>
- Tsunoda, R. T., & Cosgrove, R. B. (2001). Coupled electrodynamic in the nighttime midlatitude ionosphere. *Geophysical Research Letters*, *28*(22), 4171–4174. <https://doi.org/10.1029/2001GL013245>
- Vadas, S. L. (2007). Horizontal and vertical propagation and dissipation of gravity waves in the thermosphere from lower atmospheric and thermospheric sources. *Journal of Geophysical Research*, *112*, A06305. <https://doi.org/10.1029/2006JA011845>
- Vadas, S. L., Liu, H.-L., & Lieberman, R. S. (2014). Numerical modeling of the global changes to the thermosphere and ionosphere from the dissipation of gravity waves from deep convection. *Journal of Geophysical Research: Space Physics*, *119*, 7762–7793. <https://doi.org/10.1002/2014JA020280>
- Vincent, R. (1984). Gravity-wave motions in the mesosphere. *Journal of Atmospheric and Terrestrial Physics*, *46*(2), 119–128. [https://doi.org/10.1016/0021-9169\(84\)90137-5](https://doi.org/10.1016/0021-9169(84)90137-5)
- Walterscheid, R., Hecht, J., Vincent, R., Reid, I., Woithe, J., & Hickey, M. (1999). Analysis and interpretation of airglow and radar observations of quasi-monochromatic gravity waves in the upper mesosphere and lower thermosphere over Adelaide, Australia (35°S, 138°E). *Journal of Atmospheric and Solar-Terrestrial Physics*, *61*(6), 461–478. [https://doi.org/10.1016/S1364-6826\(99\)00002-4](https://doi.org/10.1016/S1364-6826(99)00002-4)

- Wu, Q., & Killeen, T. L. (1996). Seasonal dependence of mesospheric gravity waves (<100 km) at Peach Mountain Observatory, Michigan. *Geophysical Research Letters*, *23*(17), 2211–2214. <https://doi.org/10.1029/96GL02168>
- Yokoyama, T., Hysell, D. L., Otsuka, Y., & Yamamoto, M. (2009). Three-dimensional simulation of the coupled Perkins and Es-layer instabilities in the nighttime midlatitude ionosphere. *Journal of Geophysical Research*, *114*, A03308. <https://doi.org/10.1029/2008JA013789>
- Yue, J., Nakamura, T., She, C.-Y., Weber, M., Lyons, W., & Li, T. (2010). Seasonal and local time variability of ripples from airglow imager observations in US and Japan. *Annales Geophysicae*, *28*(7), 1401–1408. <https://doi.org/10.5194/angeo-28-1401-2010>